PHYSICAL REVIEW FLUIDS **2**, 100504 (2017)

Low-dimensional and data fusion techniques applied to a supersonic multistream single expansion ramp nozzle

Matthew G. Berry,[1,*] Cory M. Stack,[2,†] Andrew S. Magstadt,[1,‡] Mohd Y. Ali,[1,§] Datta V. Gaitonde,[2,‖] and Mark N. Glauser[1,¶]

[1]*Department of Mechanical & Aerospace Engineering, Syracuse University, Syracuse, New York 13210, USA*

[2]*Department of Mechanical & Aerospace Engineering, The Ohio State University, Columbus, Ohio 43210, USA*

(Received 6 July 2017; published 17 October 2017)

Low-dimensional models of experimental and simulation data for a complex supersonic jet were fused to reconstruct time-dependent proper orthogonal decomposition (POD) coefficients. The jet consists of a multistream rectangular single expansion ramp nozzle, containing a core stream operating at Mach number $M_{j,1} = 1.6$ and bypass stream at $M_{j,3} = 1.0$ with an underlying deck. Proper orthogonal decomposition was applied to schlieren and particle image velocimetry data to acquire the spatial basis functions. These eigenfunctions were projected onto their corresponding time-dependent large-eddy simulation (LES) fields to reconstruct the temporal POD coefficients. This reconstruction was able to resolve spectral peaks that were previously aliased due to the slower sampling rates of the experiments. Additionally, dynamic mode decomposition was applied to the experimental and LES data sets and the spatiotemporal characteristics were compared to POD.

DOI: 10.1103/PhysRevFluids.2.100504

I. INTRODUCTION

Reduced-order methods are used in the turbulence community to understand the complex dynamics of high-Reynolds-number flows and circumvent technological challenges in experiments and simulations. Statistical averaging allows fluid dynamicists to observe the fundamental flow structure, but the time-dependent information is inherently related to the spatiotemporal resolution of the measurements and computations. This paper reviews how proper orthogonal decomposition (POD) can be leveraged to pair experiments to simulations and extrapolate time-dependent information from time-independent measurements. Additionally, low-dimensional methods, including POD and dynamic mode decomposition (DMD), have been applied to these data sets to identify flow structures and turbulence mechanisms in high-Reynolds-number supersonic jets.

The use of POD in turbulence was first proposed by Lumley [1] as a mathematical construct for identifying an optimized basis set with respect to Reynolds stress characteristics. Under certain criteria, the technique identifies the most energetic coherent structures from the background turbulence. Aubry *et al.* [2] connected low-dimensional dynamics to a turbulent flow system. This reduced-order model has since been analyzed and applied to many different types of turbulent flows (see, for example, [3–6]). Research in this field showed that the time-dependent nature of the flow structure varies, meaning dominant features can have moments of intermittent activity. However,

*mgberry@syr.edu
†stack.49@osu.edu
‡Present address: Aeronautical Engineer Lockheed Martin Palmdale, CA 93550; Andrew.s.magstadt@lmco.com
§mali06@syr.edu
‖gaitonde.3@osu.edu
¶mglauser@syr.edu

accurate observation of this time-dependent activity is determined by the sampling rate and spatial measurement technique.

Adrian [7,8], in an attempt to circumvent sampling challenges, suggested linear stochastic estimation (LSE) as a way to resolve the time-dependent information. Cole *et al.* [9] were able to apply LSE to estimate instantaneous velocities within a jet shear layer. Ukeiley *et al.* [10] and Bonnet *et al.* [11] expanded upon these approaches and applied LSE to map POD eigenfunctions in order to estimate the velocity fields. This approach allows one to obtain time-resolved information from POD while substantially reducing the need to acquire full spatially resolved data. Delville *et al.* [12] used a microphone array just outside of the jet shear layer to reconstruct instantaneous velocity fields. Tinney *et al.* [13,14] applied the technique to an axisymmetric jet by reconstructing a low-dimensional estimate of the most energetic flow events and invoking an analogy with the far-field acoustics.

Flow control techniques were soon able to use POD as a means to identify an optimal basis for decomposing a perturbed flow in a particular state. Jørgensen [15] demonstrated this by applying POD to a separated flow that had been perturbed by a large upstream oscillating disturbance. Cohen *et al.* [16] used a POD-based feedback loop to control an external low-Reynolds-number flow over a cylinder. Pinier *et al.* [17] applied this closed-loop approach to prevent separation on a NACA-4412 airfoil.

Advances in experimental techniques by Wernet [18], among others, eventually allowed for time-resolved particle image velocimetry (PIV) measurements of high-subsonic jets. Berger *et al.* [19] and Low *et al.* [20] used POD-based feedback control to drive synthetic jet actuators at the nozzle lip of a Mach 0.6 axisymmetric jet. Low *et al.* then used simultaneous time-resolved PIV, near-field pressure, and far-field microphone data to identify "loud" events at the potential core collapse. Proper orthogonal decomposition was applied to the velocity field and the time-dependent coefficients were correlated to far-field pressure measurements to determine which modes had the largest impact on jet noise. The closed-loop control could then be designed to force the jet to a quieter state and decrease far-field noise.

Berger *et al.* [21] took the analysis a step further and reconstructed the time-dependent velocity field using these loud modes. This approach expanded upon work by Tinney *et al.* [14,22] and Schlegel *et al.* [23] identifying sound source mechanisms. Berger *et al.* were able to determine that the noisy events in the flow and their correlation to the far-field acoustics were related to peaks in the time-dependent POD coefficients. At these instances in time, the spatial structure of the loud mode contorts and correlates to a noisy flow event.

However, it is not possible to acquire sufficient temporal resolution of the velocity field for all flows. Even at moderate supersonic speeds, current time-resolved PIV systems face challenges in obtaining large enough ensembles to apply most low-dimensional model techniques. In these cases, we revert to other experimental methods, such as schlieren or hydrodynamic pressure measurements, as well as simulations. Time-resolved schlieren can acquire massive ensembles of images, but the measured quantities are scalars related to density gradients. Similarly, computational fluid dynamics (CFD) simulations, such as large-eddy simulations (LESs), provide highly resolved time-dependent data, but need comprehensive validation and require significant resources to obtain long records. In these cases, reduced-order models can be leveraged in conjunction with data fusion techniques to merge information between experiments and simulations. This generates a more complete view of the flow while also providing a basis for comparison.

For example, Zimmermann *et al.* [24] used CFD on an airfoil to create POD basis functions, which were fused with experimental lift and drag measurements to reconstruct the flow at different conditions. Additionally, Ruscher *et al.* [25] utilized the symmetries in the velocity field of an axisymmetric jet to repair gaps created by camera obstructions and were able to use the fused POD to reconstruct the missing information in the instantaneous flow field.

In this paper we use POD on experimental data to construct the spatial basis functions of schlieren and velocity fields for a supersonic single expansion ramp nozzle (SERN). The eigenfunctions are then projected onto a time-resolved LES of the same configuration to reconstruct the time-dependent POD coefficients. Additionally, DMD is applied to these experimental and LES data sets and the spatiotemporal characteristics are compared to POD.

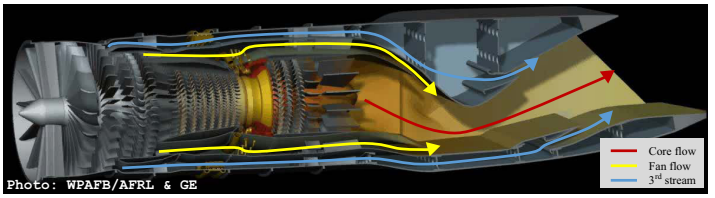

FIG. 1. Three-stream turbofan design by AFRL, WPAFB and GE.

II. CONFIGURATION

An idealized three-stream nozzle with an aft deck based on a variable-geometry engine cycle by Simmons [26] is considered. While traditional turbofans utilize a core and fan flow, the three-stream engine produces an additional bypass flow, designated the third stream. The exhaust configuration utilizes a SERN, where the gas pressure transfer occurs on only one side. The engine architecture for the three-stream turbofan collaboration between Air Force Research Laboratory, Wright-Patterson Air Force Base (AFRL, WPAFB) and General Electric (GE) can be seen in Fig. 1.

As mentioned above, we study an idealized version of the three-stream architecture, wherein we assume that the core and fan streams of Fig. 1 are fully mixed to result in the single core stream of Fig. 2, while the third stream remains in both configurations. Thus, we view this as an idealized representation of two canonical flows: a supersonic convergent-divergent (CD) jet and a sonic wall jet (representing the third stream). The main (core) stream contains the SERN and the wall jet (third stream) is a convergent bypass stream that enters the main flow in the SERN divergent section. The design operating conditions of the main and third streams have Mach numbers $M_{j,1} = 1.6$ and $M_{j,3} = 1.0$, respectively. The third stream is pulled from the core flow upstream of the CD section and throttled using a set of butterfly valves. After passing through a convergent duct, the bypass stream reenters the main flow as a wall jet.

An extended plate is outfitted on the bottom of the configuration, representing the surface of an aircraft. Additionally, the nozzle can be rotated azimuthally, creating a hemispherical observation window around it to facilitate flow field and acoustic measurements in a variety of locations. Dimensions and design conditions for the nozzle can be found in Refs. [27,28].

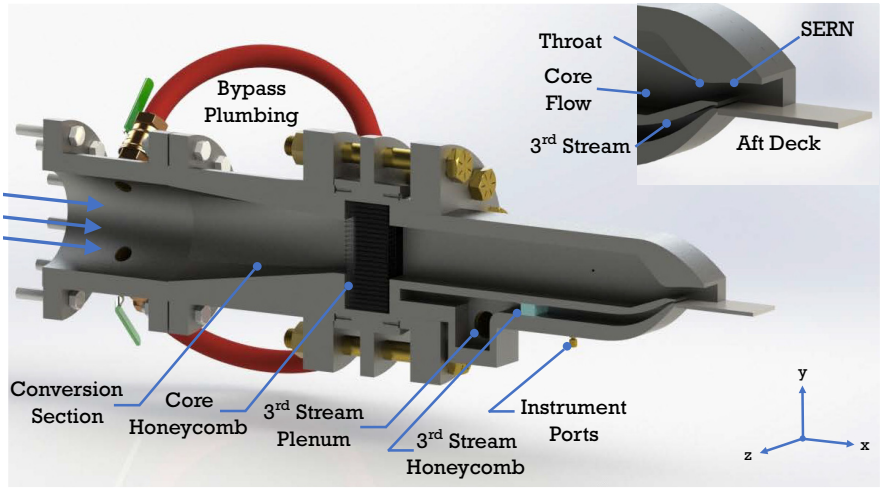

FIG. 2. Cross-sectional view of the idealized three-stream nozzle with aft deck installed at Syracuse University.

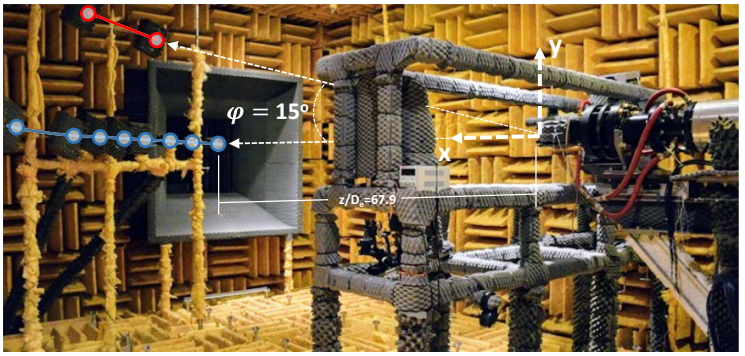

FIG. 3. Anechoic chamber showing the schlieren setup and microphone arrays with axes.

III. EXPERIMENTAL SETUP

The experiments presented herein were conducted in a $7.9 \times 6.1 \times 4.3$ m^3 anechoic chamber, acoustically treated with fiberglass wedges to achieve a cutoff frequency of ∼150 Hz (Fig. 3). The jet rig was operated by a 100-hp reciprocating Joy compressor. A 45-m^3 array of storage tanks created a blow-down facility capable of attaining supersonic jet speeds and a Reynolds number based on effective diameter $\mathrm{Re}_{D_e} \sim 2.7 \times 10^6$ for runs up to 1 min. The current coordinate system defines x as the downstream direction, y along the jets minor axis, and z along the jets major axis, as can be seen in Fig. 2.

A. Schlieren imaging

The schlieren technique utilizes optical inhomogeneities of refracted light rays to observe the flow. These optical deviations manifest as gradients proportional to the index of refraction n'. Illuminance corresponds to the first spatial derivative of the refractive index and directly relates to density gradients, in this case $\partial\rho/\partial x$. The schlieren system was arranged in a vertical Z-type configuration, seen in Refs. [29,30]. The setup utilized twin 318-mm-diam parabolic mirrors with a 2.54-m focal length and a Luminus CBT-120 green light-emitting-diode pulsed light source modeled after [31,32]. A vertically oriented knife edge set at the second focal point operated at an 80% cutoff and the camera exposure was set to 3.75×10^{-6} s. Up to 2.5×10^6 images were taken in each run with a Photron SA-Z high-speed camera. The sampling rate was a function of the viewing area. In this study we analyze results from the largest window, which allows for a sampling rate of 50 kHz and extends $x/D_h \approx 6$ from the nozzle exit, with D_h the hydraulic diameter. Results at other sampling rates can be found in Ref. [28].

B. Particle image velocimetry

Particle image velocimetry was used to capture all three velocity components at several streamwise and cross-stream planes, as seen in Ref. [33]. The work presented here will only focus on the u velocity along the nozzle's plane of symmetry (midpoint of the major axis at $z/D_h = 0$). This experiment incorporated a NewWave Gemini Nd:YAG laser and two FlowSense EO 4MP cameras to resolve all three components of velocity. Seed particles were provided by a ViCount 1300 smoke generator. To avoid condensation in the flow, the nozzle was slightly heated to ∼77 °C, bringing the core flow above the atmospheric dew point. Images were captured at 10 Hz and 2400 snapshots were acquired per plane.

IV. LARGE-EDDY SIMULATION

The full compressible Navier-Stokes equations are solved using the well-validated FDL3DI solver [34]. An implicit second-order Beam-Warming scheme with two subiterations is employed for time

integration, allowing a time step of approximately $\delta t \approx 47$ ns. Inviscid spatial fluxes are discretized using a third-order upwind-biased scheme, supplemented with a van Leer harmonic limiter to provide reliable results. Viscous fluxes are discretized with second-order central differencing. Previous results with the above methodology on numerous jets can be found in Refs. [35,36].

Nozzle exit conditions can have a significant influence on the downstream evolution of the plume and its acoustic radiation characteristics [37], thus special care must be taken in specifying these conditions. Ideally, the laminar-turbulent transition process of the interior nozzle boundary layers should be included in the simulation, but for high-Reynolds-number flows, the computational costs associated with this process is prohibitive. Instead, a turbulent inflow can be imposed on the inlet plane to avoid this costly computation. There are many varieties of turbulent inflow generation, including precursor simulations [38], recycling and rescaling methods [39,40], and synthetic turbulence [41,42]. Ultimately, a synthetic turbulence approach called digital filtering, originally proposed by Klein *et al.* [43] and further extended to compressible flows by Touber and Sandham [44], is leveraged due to the flexibility of the method to accommodate two independent rectangular streams. Additional details regarding the digital filtering routine and numerical scheme can be found in Ref. [45].

Several meshes were considered to ensure adequate resolution as discussed in Ref. [45]. Grid-independent results used in this study were obtained on a $1675 \times 705 \times 509$ mesh, corresponding to roughly 600×10^6 nodes. The grid was designed to account for the upward plume deflection as well as shear layer growth, where the deflection angle and spreading rates were guided by experiments and preliminary simulations. Further information regarding the grid, including the overall topology, and a detailed description of the node distribution may also be found in Ref. [45]. For this study, the entire flow field was sampled every 52 time steps, corresponding to 16.5 ms of physical time (roughly a 405-kHz sampling rate), with a total of 6673 snapshots. Additionally, the results are spatially downsampled to match the experimental spatial resolution.

V. BASELINE COMPARISONS

Several baseline comparisons have been made between experiments and LES in Ref. [45]. In the context of the schlieren, experiments observe the index of refraction as discussed above, while the numerical schlieren is computed using either streamwise density or pressure gradients. Both quantities are integrated across the span of the jet, consistent with the optical path visualization of the experiment.

Figure 4 shows a comparison of the time-averaged schlieren shock structures. The top image is the experiment and the bottom image is the corresponding spanwise-integrated density gradient

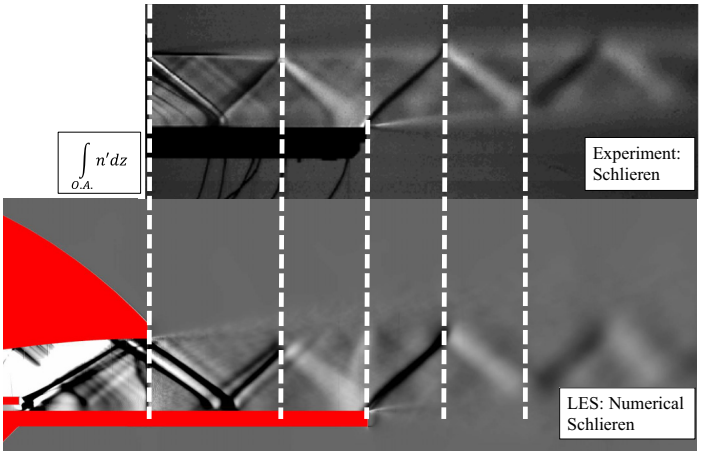

FIG. 4. Comparison of time-averaged experimental and numerical schlieren images.

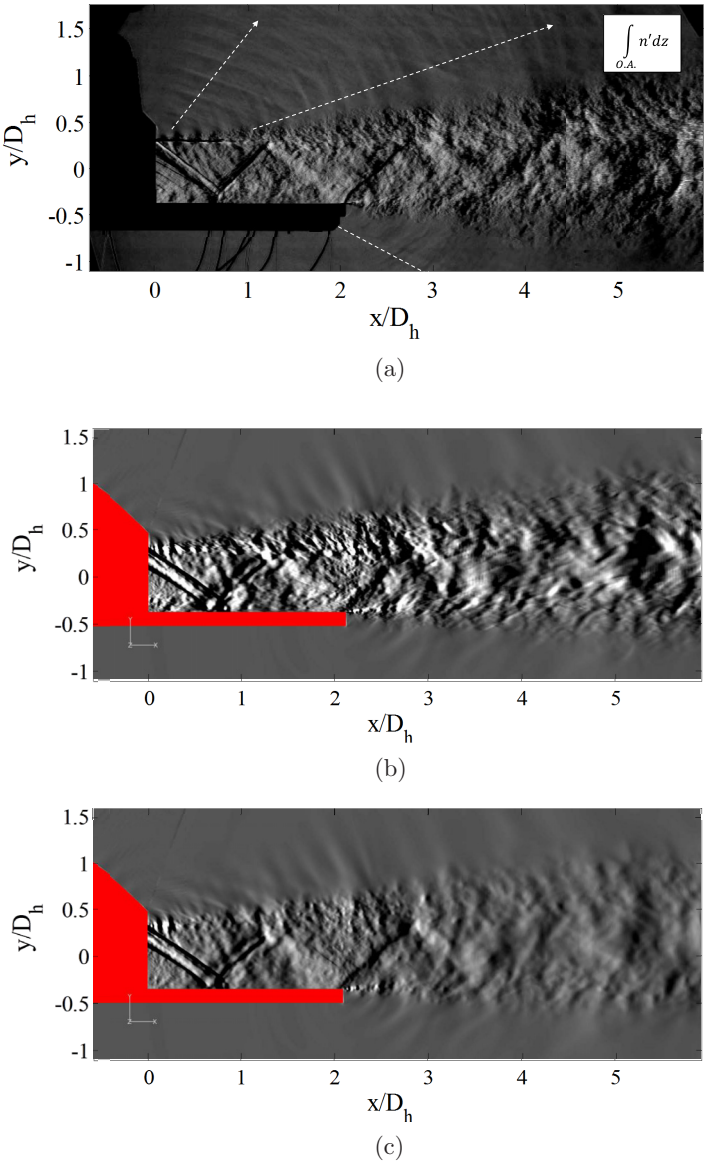

FIG. 5. Instantaneous snapshot of the experimental and LES numerical schlieren fields: (a) experimental schlieren field at an exposure of 3.75×10^{-6} s, (b) LES density gradients, and (c) LES pressure gradients.

from the LES. All quantities are averaged over several thousand snapshots. Similar shock structures emanate from the upper nozzle lip in all images. The subsequent shock reflections between the aft deck and upper shear layer are highlighted with vertical lines and match very well between the data sets. Additionally, the LES allows us to view the nozzle interior, revealing the internal oblique shock originating from the splitter plate.

Figure 5 shows an instantaneous snapshot of the experimental and LES schlieren images. Figure 5(a) shows the experimental observation, Fig. 5(b) shows the streamwise LES density gradients ρ_x, and Fig. 5(c) shows the streamwise LES pressure gradients P_x. Figure 5(a) observes a pair of neighboring oblique shocks emanating from the nozzle exit and reflecting between the aft

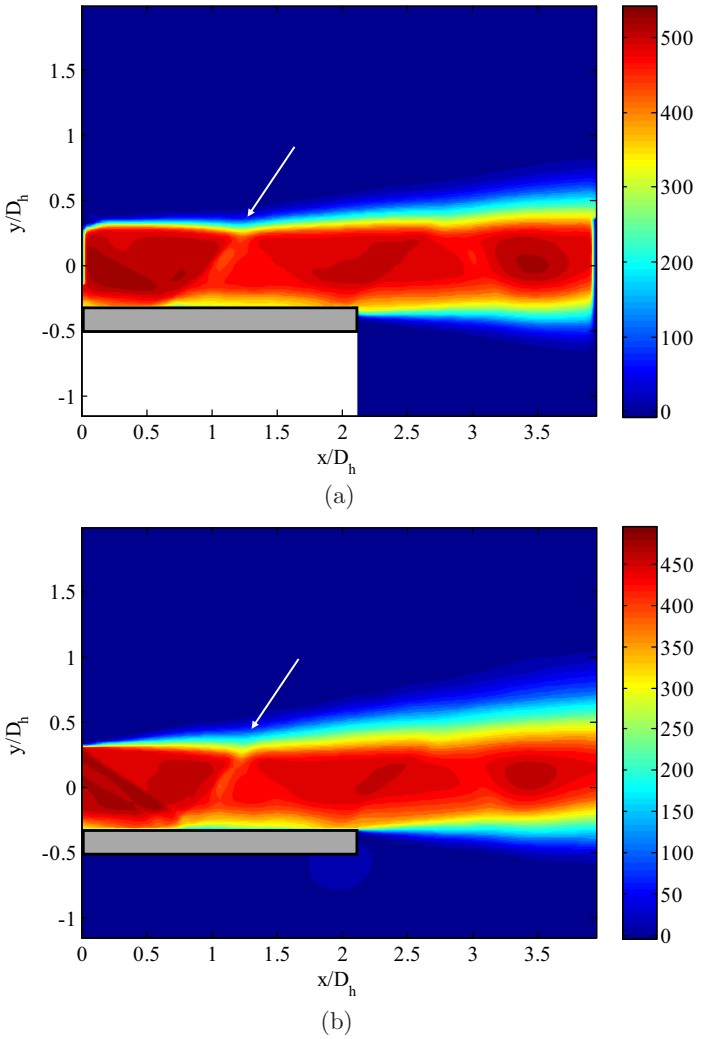

FIG. 6. Time-averaged u velocity of PIV and LES fields along the centerline plane ($z/D_h = 0$): (a) PIV average u velocity (m/s) and (b) LES average u velocity (m/s).

deck and upper shear layer. The same two shocks are seen in Figs. 5(b) and 5(c), but the spacing of these shocks is larger in the LES.

Additionally, Fig. 5(a) shows three separate bands of acoustic propagation, marked with dotted lines. One occurs at the nozzle lip, along with one where the reflected oblique shock interacts with the upper shear layer and one at the bottom trailing edge of the aft deck. Traces of acoustic propagation can be seen in Figs. 5(b) and 5(c) near the intersection point of the reflecting oblique shock and upper shear layer, as well as from the aft deck trailing edge.

Figure 5(a) depicts sets of periodic structures propagating along the upper shear layer and along the aft deck near the nozzle exit. The results shown in Figs. 5(b) and 5(c) contain these same structures, with the addition of another at the aft deck trailing edge. As expected due to the coupling of the pressure and density, many of the flow characteristics are similar between the LES quantities, but the contours show lower feature resolution in the pressure field.

Figure 6 shows the time-averaged streamwise velocity in m/s along the centerline plane of the jet. Figure 6(a) shows the experiment and Fig. 6(b) shows the LES. Traces of the oblique shocks can

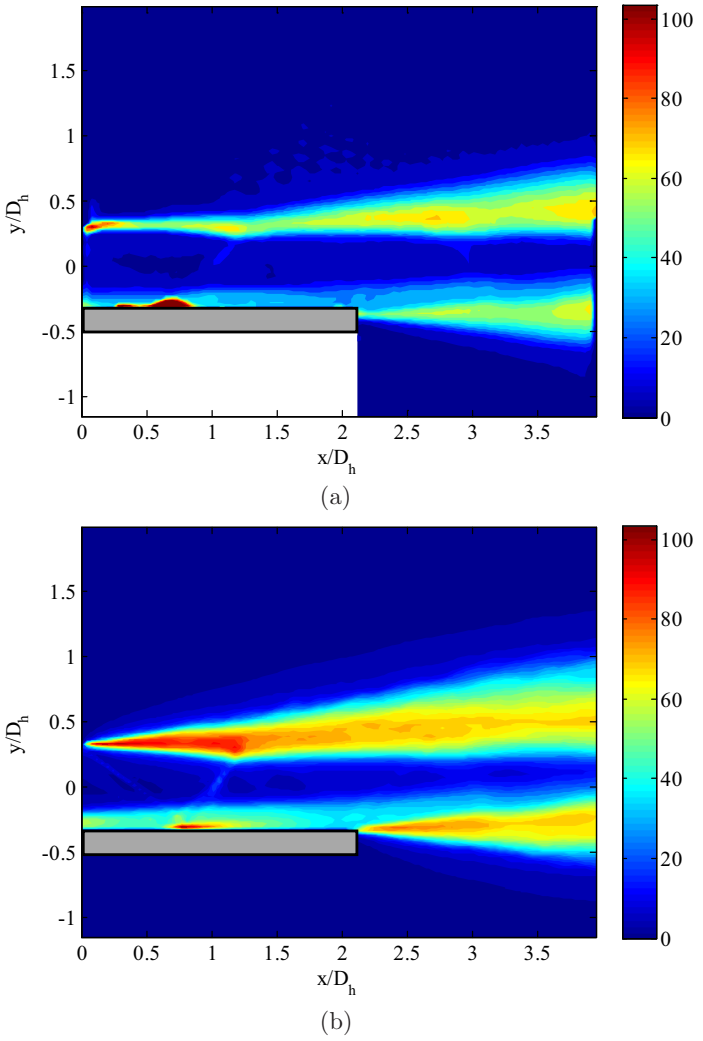

FIG. 7. The rms u velocity of PIV and LES fields along the centerline plane ($z/D_h = 0$): (a) PIV rms u velocity (m/s) and (b) LES rms u velocity (m/s).

be seen emanating from the upper nozzle lip and reflecting between the aft deck and upper shear layer. Additionally, there is a change in growth rate where the oblique shock interacts with upper shear layer, marked with an arrow. A region of lower average velocity is evident along the deck just downstream of the reflecting shock. Deck pressure measurements by Berry *et al.* [46] and LES results by Stack and Gaitonde [45] indicate that the deck boundary layer separates downstream of the impinging shocks, but reattaches before the end of the plate. Due to flaring laser reflections on the aft deck, some of the boundary layer close to the wall is not captured by the PIV setup. Downstream of the aft deck, both the PIV and LES show an upward deflection of the jet plume.

The centerline plane rms streamwise velocity is presented in Fig. 7 in m/s. Figure 7(a) shows the PIV experiment and Fig. 7(b) shows the LES. Both figures show a region of high fluctuations along the aft deck just downstream of the reflecting oblique shock, highlighting the separated region and eventual downstream recovery. Additionally, the rms highlights differences in shear layer growth before and after the reflecting oblique shock interacts with the upper shear layer at $x/D_h \approx 1.25$. This shock-shear layer interaction creates a wake region that enhances mixing and promotes shear

layer growth. The experimental rms indicates smaller fluctuations in the separation region than the LES, but much more rapid growth of the shear layers. There remains a change in shear layer growth and direction downstream of the shock reflection in the LES, but the shear layer is already much thicker before this location. As observed in Fig. 5, the upward vectoring of the plume downstream of the aft deck is evident in the rms. Data from the PIV are currently being used to develop more realistic boundary conditions at the nozzle exit.

VI. LOW-DIMENSIONAL METHODS

A. Proper orthogonal decomposition

Proper orthogonal decomposition has become a well-established method to find optimal basis functions by identifying the structures with largest mean-square projection. Proper orthogonal decomposition determines the optimal basis functions by maximizing the mean-square projection of the system using a spatial two-point correlation tensor in an eigenvalue problem.

The technique was later modified by Sirovich [47], who redefined the problem in time rather than space, making calculations manageable for highly resolved spatial data, such as those obtained from PIV, schlieren, and LES. For completeness, a brief summary of the snapshot POD process is described.

The objective is to decompose a spatiotemporal field into time-dependent coefficients and spatial basis functions. In this derivation, velocity components are represented by u_i. An additional derivation using the index of refraction n' can be found in Ref. [28]. The method first calculates the integral eigenvalue problem defined by

$$\frac{1}{T}\int_T C(t,t')a_n(t')dt' = \lambda^{(n)}a_n(t), \tag{1}$$

where T is the integration time represented by the number of snapshots, $a_n(t)$ is the temporal eigenfunction, and $C(t,t')$ is the two-time correlation tensor, defined by

$$C(t,t') = \int_{\mathcal{D}} u_i(\vec{x},t)u_i(\vec{x},t')d\vec{x}, \tag{2}$$

where $\mathcal{D}$ is the spatial domain of interest. In order to maintain the analogy between classical and snapshot POD, the temporal coefficients are scaled to their corresponding eigenvalues

$$\langle a_m(t),a_n(t)\rangle = \lambda^{(m)}\delta_{mn}, \tag{3}$$

where $\langle\cdot,\cdot\rangle$ represents the inner product and δ_{mn} is the Kronecker delta. Finally, the spatial eigenfunctions $\phi_i^{(n)}(\vec{x})$ are defined by

$$\phi_i^{(n)}(\vec{x}) = \frac{1}{T\lambda^{(n)}}\int_T a_n(t)u_i(\vec{x},t)dt. \tag{4}$$

The original velocity field can be perfectly reconstructed using N modes (where N is the number of snapshots) of the temporal coefficients and basis functions, or partially using a subset of the modes

$$u_i(\vec{x},t) = \sum_{n=1}^{N} a_n(t)\phi_i^{(n)}(\vec{x}). \tag{5}$$

In turbulence research, experiments commonly generate a large number of statistically independent snapshots that are not necessarily time resolved, while computations have a small number of statistically independent snapshots that are time resolved. In the context of POD, these traits lead to better converged basis functions in experiments due to the statistical independence of the snapshots and better resolved temporal coefficients using computational data from the enhanced temporal resolution. Furthermore, when utilizing a time-resolved data set, the snapshots are often downsampled in time to maintain statistical independence between them. Once the spatial and

temporal components are computed (using the downsampled data), the original data set is then projected onto the basis functions from the downsampled data $\phi_i^{(n)}(\vec{x})$ to recompute the time-resolved temporal coefficients $a_n(t)$. This approach promotes statistically independent snapshots for the computation of the spatial eigenfunctions while maintaining the original temporal resolution of the data set.

While snapshot POD applications are typically performed on velocity vectors, others have applied POD to scalar fields as well [48–51]. Schlieren images provide a two-dimensional visualization of the three-dimensional flow field due to the path-integrated nature of the technique and the visualized quantities have different physical dimensions than velocity components. When POD is performed on a velocity data set, all structures within the flow are separated by their energy contents $[(\mathrm{m/s})^2]$. In the case of schlieren, POD modes are ordered by the square of the density gradient $(d\rho/dx)^2$, given in units of $(\mathrm{kg/m^4})^2$. Such quantities will be further referred to as the mean-square value.

B. Dynamic mode decomposition

Dynamic mode decomposition is related to the Koopman modes obtained by the classical Arnoldi algorithm, seen in Ref. [52]. The DMD algorithm used in the present work was adapted from [53]. The data set is a time-resolved record of velocity fields sampled at a frequency f_s sufficiently higher than the Nyquist criterion. A temporal sequence of N velocity fields, consisting of column vectors $\mathbf{v}_j$ that are equispaced in time, can be written as

$$\mathbf{V}_1^N = \{\mathbf{v}_1, \mathbf{v}_2, \mathbf{v}_3, \ldots, \mathbf{v}_N\}. \tag{6}$$

The primary basis of the method is that each velocity field snapshot $\mathbf{v}_j$ is connected to a subsequent velocity field $\mathbf{v}_{j+1}$ by a linear mapping $\mathbf{A}$ such that

$$\mathbf{v}_{j+1} = \mathbf{A}\mathbf{v}_j, \tag{7}$$

where $\mathbf{A}$ is approximately the same over the full data set. The eigenvalues and eigenvectors of the matrix $\mathbf{A}$ characterize the behavior of the dynamical system. The constant mapping assumption of the dynamical system $\mathbf{A}$ between the velocity field sequence allows us to formulate a Krylov sequence of the data

$$\mathbf{V}_1^N = \{\mathbf{v}_1, \mathbf{A}\mathbf{v}_1, \mathbf{A}^2\mathbf{v}_1, \ldots, \mathbf{A}^{N-1}\mathbf{v}_1\}. \tag{8}$$

As the number of velocity fields increases, the data set is assumed to approach a linear dependence. The last velocity field vector $\mathbf{v}_N$ can be expressed as a linear combination of the previous linearly independent vectors

$$\mathbf{v}_N = a_1\mathbf{v}_1 + a_2\mathbf{v}_2 + \cdots + a_{N-1}\mathbf{v}_{N-1} + \mathbf{r}, \tag{9}$$

where $\mathbf{r}$ is the residual vector. Equation (9) can be written in a matrix form

$$\mathbf{v}_N = \mathbf{V}_1^{N-1}\mathbf{a} + \mathbf{r}, \tag{10}$$

where the coefficients $\mathbf{a}^T = \{a_1, a_2, \ldots, a_{N-1}\}$ can be obtained using the least-squares method. Following [54], Eq. (10) can be written in the form of two lagged matrices

$$\mathbf{A}\{\mathbf{v}_1, \mathbf{v}_2, \ldots, \mathbf{v}_{N-1}\} = \{\mathbf{v}_2, \mathbf{v}_3, \ldots, \mathbf{v}_N\} = \left\{\mathbf{v}_2, \mathbf{v}_3, \ldots, \mathbf{V}_1^{N-1}\mathbf{a}\right\} + \mathbf{r}\mathbf{e}_{N-1}^T, \tag{11}$$

where $\mathbf{e}_{N-1}$ is the $(N-1)$th unit vector. Equation (11) can be written in a matrix form

$$\mathbf{A}\mathbf{V}_1^{N-1} = \mathbf{V}_2^N = \mathbf{V}_1^{N-1}\mathbf{S} + \mathbf{r}\mathbf{e}_{N-1}^T. \tag{12}$$

The matrix $\mathbf{S}$ in Eq. (12) is of the companion type

$$\mathbf{S} = \begin{pmatrix} 0 & & & & a_1 \\ 1 & 0 & & & a_2 \\ & \ddots & \ddots & & \vdots \\ & & 1 & 0 & a_{N-2} \\ & & & 1 & a_{N-1} \end{pmatrix}, \tag{13}$$

which shifts the data set index from 1 to $N-1$. The number of velocity fields N can be increased until the residual $\mathbf{r}$ converges. The matrix $\mathbf{S}$ is a low-dimensional representation of the full system matrix $\mathbf{A}$. The eigenvalues λ_j of matrix $\mathbf{S}$ approximate some of the eigenvalues of the full system matrix $\mathbf{A}$ [53], which are also referred to as the Ritz values [52].

The companion matrix $\mathbf{S}$ is computed by calculating the singular value decomposition of the data matrix $\mathbf{V}_1^{N-1}$,

$$\mathbf{V}_1^{N-1} = \mathbf{U}\Sigma\mathbf{W}^H. \tag{14}$$

Substituting Eq. (14) into (12) and neglecting the residual term, we get

$$\mathbf{V}_2^N = \mathbf{U}\Sigma\mathbf{W}^H\mathbf{S} \tag{15}$$

and the approximate full matrix

$$\tilde{\mathbf{S}} = \mathbf{U}^H\mathbf{V}_2^N\mathbf{W}\Sigma^{-1} = \mathbf{U}^H\mathbf{A}\mathbf{U}, \tag{16}$$

which is obtained by projecting $\mathbf{A}$ onto $\mathbf{U}$. The matrix $\mathbf{U}$ contains the POD basis and forms the right singular vector of the data matrix $\mathbf{V}_1^{N-1}$. The eigenvalue decomposition of the matrix $\tilde{\mathbf{S}}$ gives the eigenvalues λ_j and eigenvectors $\mathbf{y}_j$ such that $\tilde{\mathbf{S}}\mathbf{y}_j = \lambda_j\mathbf{y}_j$. Finally, the dynamic modes are computed as

$$\mathbf{\Phi}_j = \mathbf{U}\mathbf{y}_j. \tag{17}$$

The approximate eigenvalues (Ritz values) λ_j can be used to study the stability characteristics of the computed DMD modes. The eigenvalues occur as complex conjugate pairs and lie on a unit circle in the complex domain representing the modes with zero-growth rates. The eigenvalues lying inside and outside the unit circle represent the damped and undamped modes, respectively. Furthermore, the eigenvalues can be mapped logarithmically as

$$\omega_j = \ln(\lambda_j)/\Delta t, \tag{18}$$

where $\Delta t = f_s^{-1}$ is the separation time between successive velocity fields. The discrete frequencies of the decomposed data f_j are determined from the imaginary part of the logarithmically mapped eigenvalues as

$$f_j = 2\pi\ \mathrm{Im}\{\omega_j\} = \arg(\lambda_j)/2\pi\,\Delta t. \tag{19}$$

The negative frequencies are neglected and each mode pair is identified by the positive-value frequency. The mean feature is a special mode where the imaginary component of the eigenvalue is zero, indicating that it is invariant in time. Beyond the zero-frequency case, the DMD modes can be sorted by their amplitudes $\|\Phi\|$.

Dynamic mode decomposition is closely related to the more commonly used POD modes. The singular value decomposition of the data matrix $\mathbf{V}_1^{N-1}$ contains the spatial structures $\phi^n(\vec{x})$, the eigenvalues (diagonal matrix Σ), and the time-dependent coefficients $a_n(t)$. In POD, spatial orthogonality of the identified structures is enforced, allowing multiple frequencies in each individual

POD mode. However, DMD is orthogonal in time, thus each mode is identified with a single frequency.

VII. ANALYSIS

A. Schlieren results

Figure 8(a) displays the first nine spatial eigenfunctions of the refractive index $\phi^{(n)}(\vec{x})$ sorted in descending order of mean-square value. The eigenfunction contours are scaled by the total mean-square content in each respective mode. The viewing area of this window extends from slightly upstream of the nozzle exit to $x/D_h \approx 5.5$. Modes 1 and 2 exhibit near-field acoustics along with distinct structures emanating from the nozzle lip and along the aft deck. Snapshot POD oftentimes pairs sequential modes 90° out of phase with one another. This phase relationship is tied to the propagation of the structures through the field and manifests itself as modes with similar spatial and spectral content. The structures in modes 1 and 2 have been associated with a Kelvin-Helmholtz (KH) instability at the intersection of the main and bypass streams, as seen in Refs. [45,46,55]. These structures travel along the aft deck in the mixing layer and interact with the trailing edge of the plate to generate the radiation evident below the nozzle. Additionally, pressure fluctuations from the KH instability travel along the shock between the splitter plate and SERN (Fig. 4) and propagate through the upper shear layer and down the first oblique shock. Modes 3 and 4 capture the shock structure and large-scale flapping downstream of the aft deck. Modes 5–9 are dominated by large-scale structures downstream, as the plume appears to transition from a flapping mode to a column mode.

Figure 8(b) displays the first nine spatial eigenfunctions of the streamwise density gradients ρ_x. Modes 1 and 4 observe a shock structure originating from the upper lip and reflecting off the aft deck. This is similar to but less complete than the shock train in the experimental data. Modes 2 and 3 exhibit similar features associated with the KH instability, namely, structures where the upper shear layer is initiated, along with traces of acoustic propagation. Additionally, small-scale structures near the bottom edge of the aft deck are visible in modes 2, 3, and 9, as also seen in experimental modes 1 and 2. Modes 4–9 closely resemble the large structures propagating downstream in the experimental data; however, these structures persist along the entire upper shear layer for the density gradients, while the experimental schlieren only showed them downstream of the aft deck. Remnants of the shock train can also be seen in the higher modes as they transition to an apparent column mode in mode 9.

Figure 8(c), utilizing streamwise pressure gradients P_x, resolves less of the downstream flow field in the first nine POD modes relative to those in Fig. 8(b). As previously observed with the density gradients, the oblique shocks emanate from the nozzle lip and reflect off the aft deck in modes 1 and 4. Also like the density gradients, the shock train is less prominent in the downstream region than the corresponding experimental modes. The same features associated with the KH instability are present in modes 2 and 3, where structures emanate from the upper lip and the trailing edge of the aft deck. The structures at the formation of the upper shear layer appear to dominate most of the observed modes. Like the above observations, remnants of the shock structure persist in the higher modes. Modes 8 and 9 show slight traces of acoustic propagation from the nozzle lip and trailing edge of the aft deck.

Due to the complexity of the schlieren fields and multitude of scales, the convergence rate of POD applied to such fields are extremely slow, as shown in Ref. [46]. Since the LES yields few statistically independent snapshots, POD of the numerical schlieren is unable to resolve some of the flow structures observed in the experimental basis functions as discussed above.

Figure 9(a) shows the power spectral density (PSD) of the time-dependent POD coefficients for the experimental schlieren. The previous schlieren, near-field pressure, far-field microphone, and LES results have shown this jet to contain a dominant 34-kHz frequency throughout the entire flow field [27,30,45,46,55]. As stated previously, this frequency is associated with a KH instability at the intersection of the main and bypass streams. However, due to the 50-kHz sampling rate of the

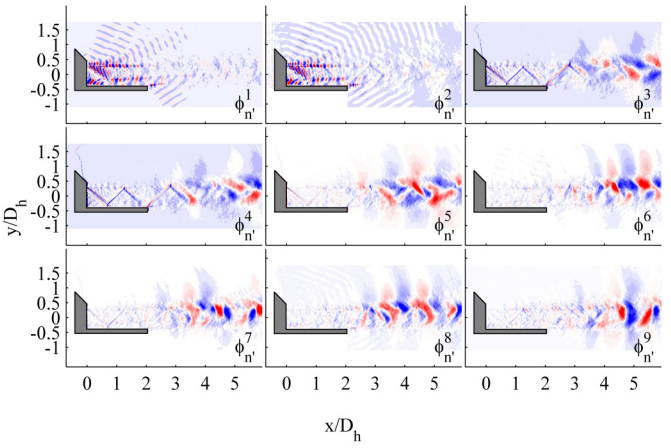

FIG. 8. Spatial POD eigenfunctions on the x-y plane for the (a) schlieren experiment, (b) LES density gradients, and (c) LES pressure gradients.

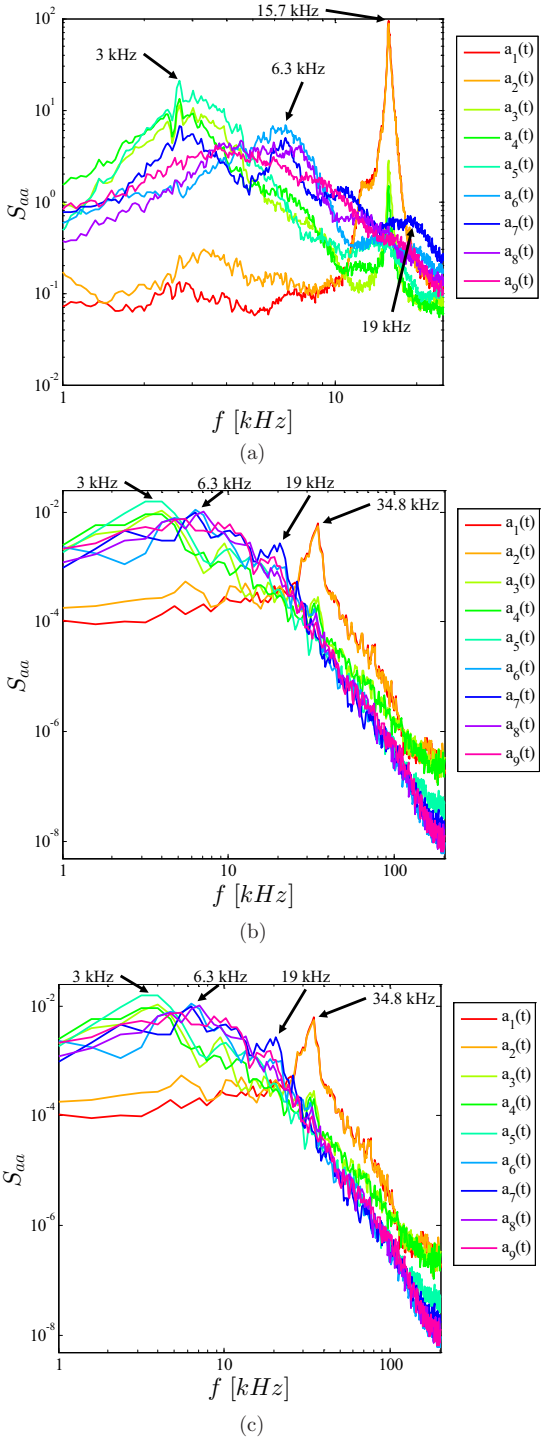

FIG. 9. Power spectral density of $a_n(t)$: (a) schlieren $a_n(t)$ spectra sampled at 50 kHz, (b) reconstructed $a_n(t)$ spectra using LES density gradients sampled at 405 kHz, and (c) reconstructed $a_n(t)$ spectra using LES pressure gradients sampled at 405 kHz.

schlieren window, the time-dependent information of the experiment is aliased, and Fig. 9(a) shows the dominant 34-kHz KH instability at 15.7 kHz. This is confirmed as the Nyquist frequency for this sample rate.

Assuming similarities between the LES and experimental flows, we can leverage strengths from both to resolve time-dependent field information as discussed in Sec. VI A. Substituting the experimental POD eigenfunction $\phi^{(n)}(\vec{x})$ as the spatial structure and the time-dependent LES fields $\rho_x(\vec{x},t)$ and $P_x(\vec{x},t)$ as the schlieren snapshots, we can then reconstruct new time-dependent POD coefficients $a_n(t)$ using Eq. (5).

Figures 9(b) and 9(c) show the reconstructed time-dependent POD coefficients $a_n(t)$ using the aforementioned procedure. The previously aliased peak at 15.7 kHz, from the 50-kHz experimental sample rate, has been properly resolved to 34.8 kHz. This peak is consistent with observations in other experiments, including schlieren measurements sampled at 100 and 400 kHz. Similar trends are detected in the lower frequencies between the experimental and reconstructed coefficients. A broadband peak around 3 kHz is evident in all of the modes except 1 and 2, as well as a broadband peak around 6.3 kHz in several modes. Additionally, a broadband peak at 19 kHz can be seen in modes 7–9. This peak falls to the right of the dominant 15.7-kHz peak in the experimental data, but can now be seen to the left of the reconstructed 34.8-kHz peak. This analysis demonstrates how reconstructing the time-dependent POD spectra only varies the frequency information of aliased data. General amplitude trends between modes also hold constant in the reconstruction.

Both the density and pressure gradients accurately resolve the dominant 34-kHz peak. However, the reconstructed spectra using the density gradients show slightly sharper peaks at the midrange frequencies. Furthermore, the amplitudes are different because the experimental schlieren use arbitrarily scaled light intensity units and the numerical schlieren are units of density and pressure.

Since the schlieren and LES data sets are relatively time resolved, DMD can be leveraged to identify structures based on their growth rate and frequency. Figure 10(a) shows the frequency-amplitude plot of the DMD modes extracted from the schlieren experiment. Similar frequencies to the time-dependent POD coefficients are observed in the DMD analysis, where the aliased KH instability is again observed at 14.7 kHz, along with peaks around 3 and 6 kHz.

Dynamic mode decomposition was also applied to the numerical schlieren. Figures 10(b) and 10(c) show the peak frequencies and associated amplitudes extracted from the respective streamwise density and pressure gradients. Both figures indicate high-frequency peaks at $\sim$30 and 36 kHz, which are in the range of the KH instability seen in the time-dependent POD spectra [Figs. 9(b) and 9(c)]. Both plots also show broader peaks around 7 and 1 kHz.

Figure 11(a) shows the spatial DMD modes for several of the peak frequencies in Fig. 10(a). Large-scale flapping structures are present in the 3-kHz mode, which are similar to structures found using POD (Fig. 8). We can quantitatively compare the similarities between the experimental POD and DMD modes using Fig. 12(a), which shows the spatial correlation between each extracted DMD mode and the first several POD modes. A 50% correlation is observed between the 3-kHz DMD mode and mode 3 of the POD, along with a 30% correlation between DMD modes 15–16 kHz [Fig. 11(a)] and the first 2 POD modes [Fig. 8(a)]. These modes are capturing the features associated with the aliased KH instability.

Dynamic mode decomposition was also performed on the numerical schlieren, and the spatial modes are shown in Figs. 11(b) and 11(c). Comparing to Figs. 8(b) and 8(c), we see the shock structure in the 1-kHz DMD mode mirrors modes 1 and 4 of the POD, which is quantified in the spatial correlations in Figs. 12(b) and 12(c). The 1- and 2-kHz modes extracted from the DMD have a 90% correlation to POD mode 1 in both cases. Figure 12(b) also shows a 40% correlation between the 8-kHz DMD mode and POD mode 5. The DMD spatial modes show smaller-scale structures in the upper shear layer over the aft deck and in the lower shear layer. Figure 12(c) shows that POD mode 3 [Fig. 8(c)] has a 50% correlation to DMD modes of 29 and 36 kHz [Figure 11(c)]. These modes show the high-frequency structures in the upper shear layer created by disturbances from the KH instability.

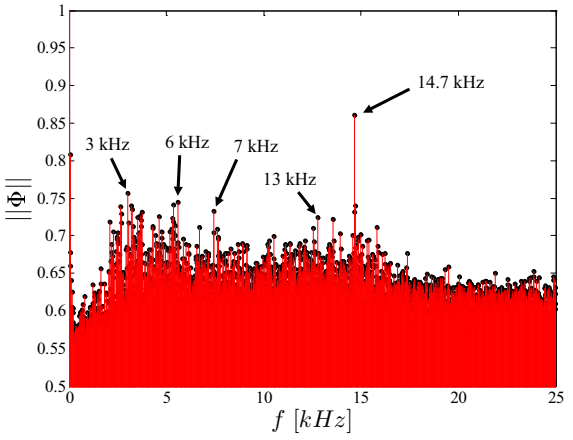

(a)

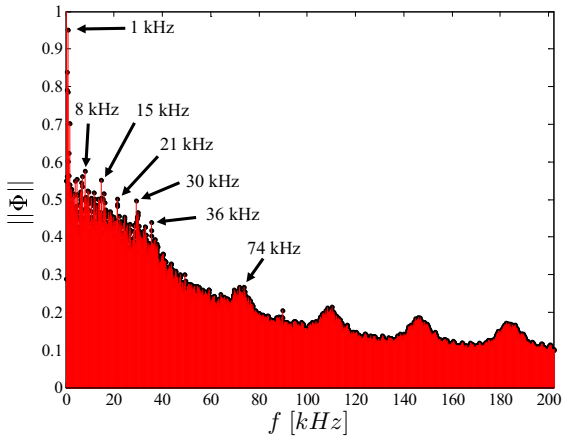

(b)

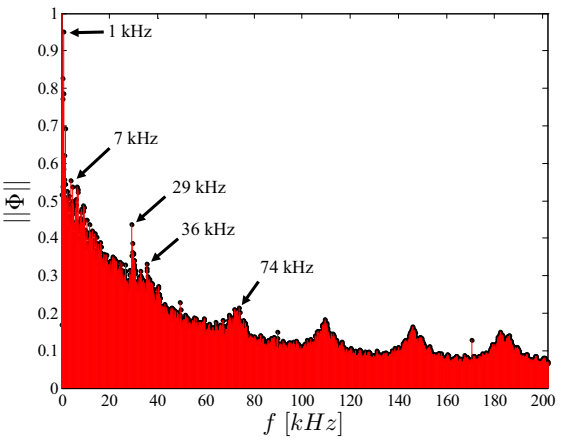

(c)

FIG. 10. The DMD frequencies of experimental and numerical schlieren fields: (a) schlieren experiment sampled at 50 kHz, (b) LES numerical schlieren using density gradients sampled at 405 kHz, and (c) LES numerical schlieren using pressure gradients sampled at 405 kHz.

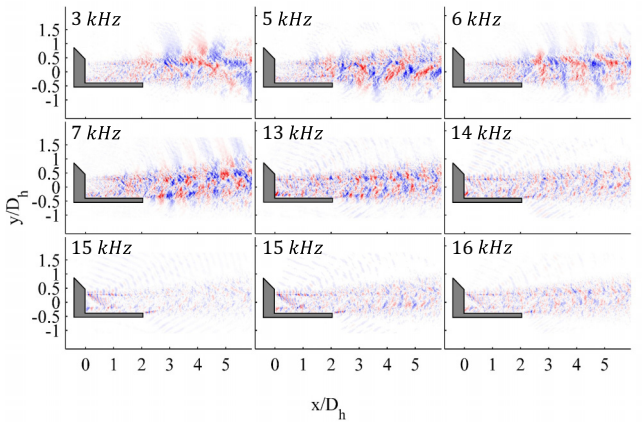

(a)

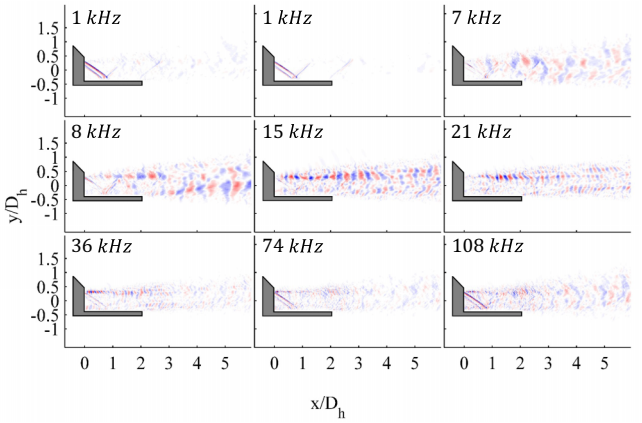

(b)

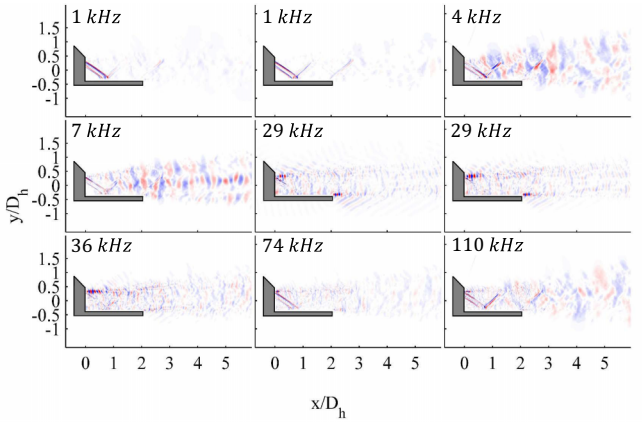

(c)

FIG. 11. The DMD spatial modes of experimental and numerical schlieren fields: (a) DMD spatial structure of the schlieren experiment, (b) DMD spatial structure of LES numerical schlieren using density gradients, and (c) DMD spatial structure of LES numerical schlieren using pressure gradients.

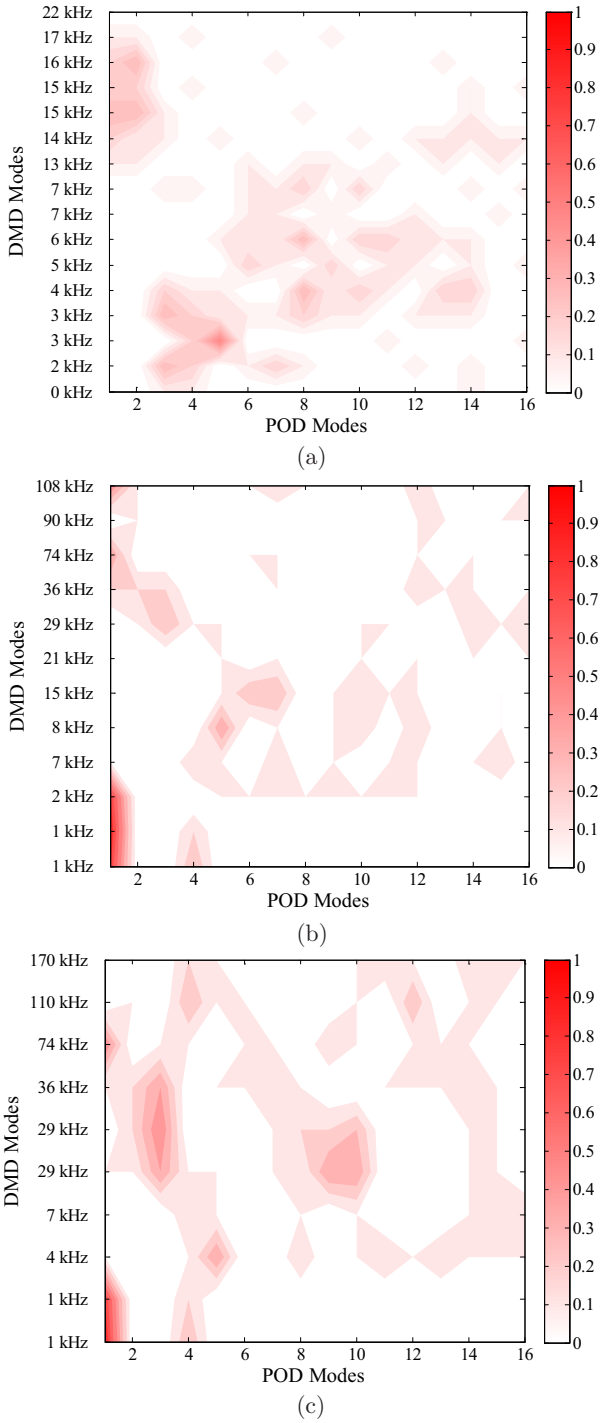

FIG. 12. Spatial correlation between DMD and POD modes for experimental and LES numerical schlieren: (a) schlieren experiment, (b) LES numerical schlieren using density gradients, and (c) LES numerical schlieren using pressure gradients.

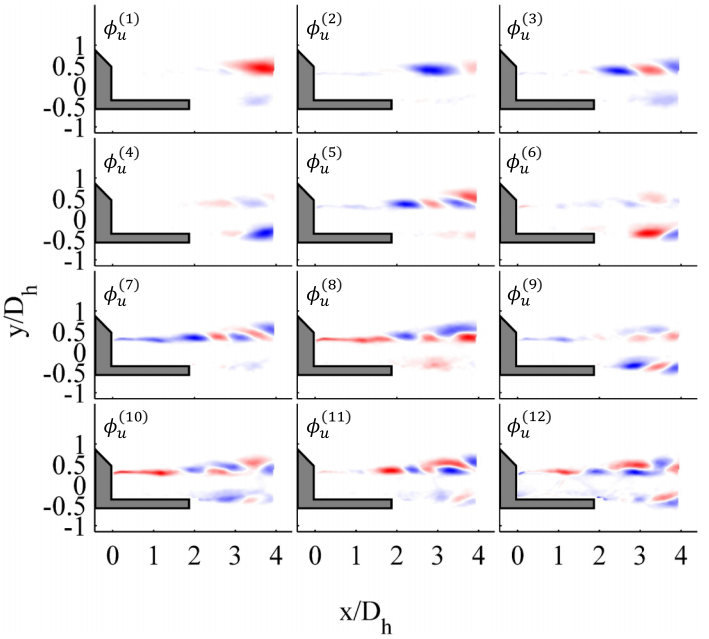

FIG. 13. The PIV modes of the *u* component.

B. Particle image velocimetry results

Stereo PIV measurements were taken along the centerline plane and POD was subsequently performed only on the streamwise component of the velocity field. The viewing window begins slightly upstream of the nozzle exit plane and extends four hydraulic diameters downstream.

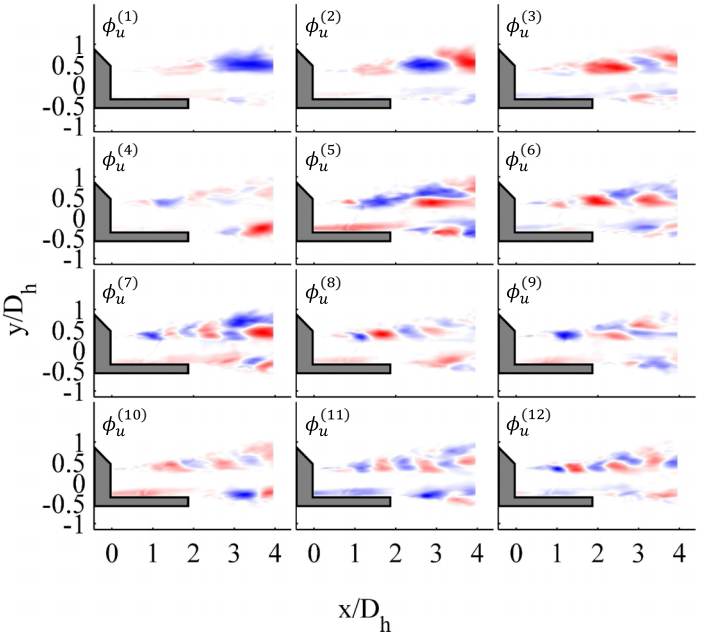

FIG. 14. The LES modes of the *u* component.

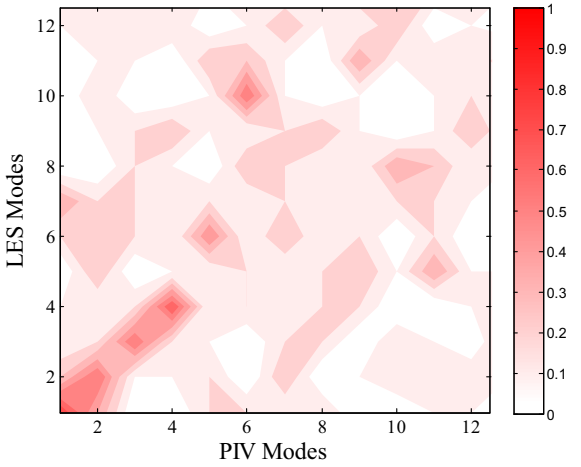

FIG. 15. Spatial correlation between LES and PIV POD modes.

Figure 13 shows the first 12 spatial eigenfunctions from the POD. Modes 1 and 2 show large-scale structures beginning downstream of the aft deck in the upper shear layer. As the mode number increases, smaller structures in the upper shear layer are observed further upstream. Additionally, a large-scale structure is evident in the bottom shear layer after the edge of the aft deck in modes 4, 6, 9, 10, and 12. Note that some of the boundary layer near the aft deck was masked out due to laser reflections that saturated the camera's CCD.

Proper orthogonal decomposition was also performed on the LES velocity field, where the LES results were interpolated to match the respective PIV spatial distribution. Figure 14 shows the first 12 spatial eigenfunctions for the POD. Several similarities are observed between the POD analyses. Modes 1 and 2 have similar large-scale structures in the upper shear layer beginning downstream of the aft deck. Similar to the experiment, as the mode number increases, smaller structures in the upper shear layer can be seen further upstream. However, the LES is able to identify a long thin flow structure in several modes along the deck surface that is not seen in the PIV due to the

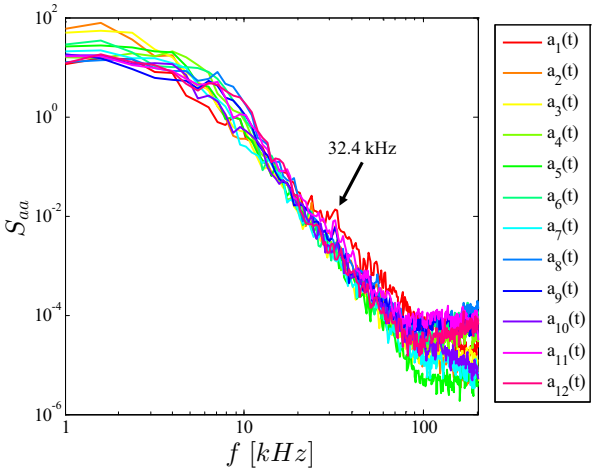

FIG. 16. Power spectral density of reconstructed $a_n(t)$ using LES u-velocity snapshots and the PIV spatial eigenfunction.

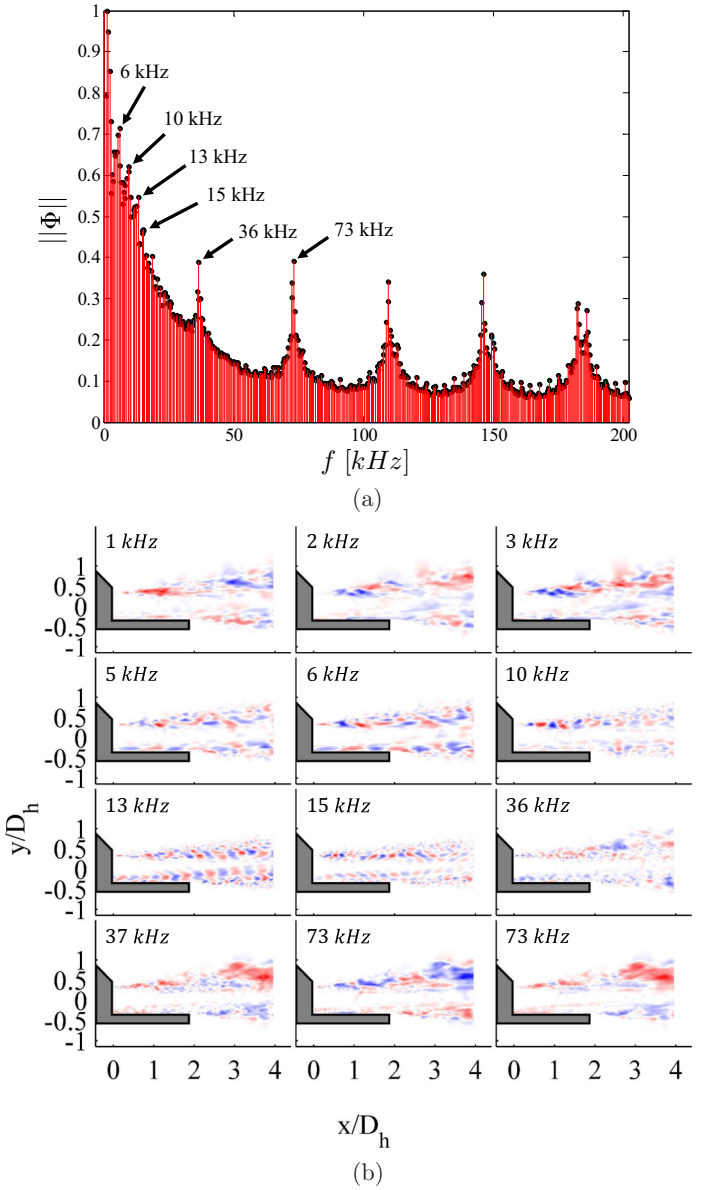

FIG. 17. The DMD of the LES u velocity field: (a) DMD frequencies of the LES u velocity and (b) DMD spatial structure of the LES u velocity.

laser reflections. This thin structure could be associated with the mixing layer that forms due to the addition of a bypass stream.

Figure 15 shows the spatial correlation between the dominant PIV and LES POD modes. The 6673 snapshots from the LES, despite lacking statistical independence, appear to resolve several of the highest-energy POD modes. Modes 1–4 are all highly correlated between the experiment and LES, with values of 80%, 60%, 60%, and 70% respectively. Additionally, mode 6 from the PIV has a 70% correlation to mode 10 of the LES. Differences between the velocity fields may be attributed to the nozzle temperature ratios (NTRs), as the streams were slightly heated to acquire PIV measurements (NTR approximately equal to 1.2), but the LES and schlieren visualizations were both

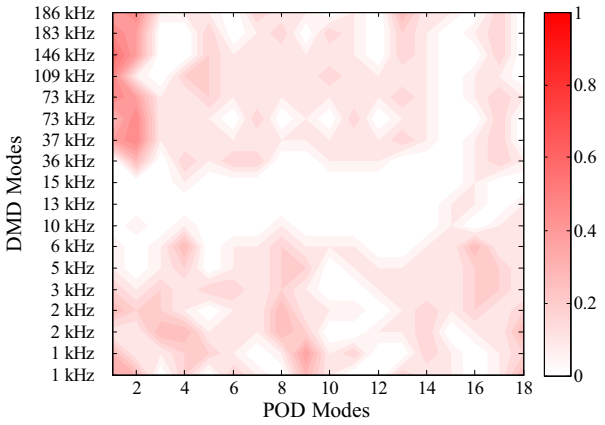

FIG. 18. Spatial correlation between the DMD and POD modes of the LES u-velocity field.

acquired at a NTR equal to 1.0. This may alter the spacing and placement of flow structures, as well as affecting spatial correlations, but the highest-energy structures appear to be independent of the slight temperature difference. Additionally, the lack of statistical independence in the LES does not affect the u-velocity decomposition as much as the schlieren, since the energy convergence is more rapid. It is clear that masking out the PIV's laser reflection along the aft deck does conceal structures in that region, which also affects the spatial correlation between the experiment and simulation.

The POD coefficient reconstruction was also performed on the velocity data sets. Assuming similarities between the PIV and LES, we substitute the experimental POD eigenfunctions $\phi_u^{(n)}(\vec{x})$ as the spatial structure and the time-dependent LES field $u(\vec{x},t)$ as the velocity snapshots and reconstruct $a_n(t)$ using Eq. (5). Since the PIV was acquired at 10 Hz, no temporal information can be extracted for comparison to the reconstruction.

Figure 16 shows the PSD of the reconstructed u-velocity temporal coefficients. Overall, the spectra of the velocity coefficients are much less tonal than the schlieren. Additionally, a small peak is observed around 34 kHz, indicating that the reconstruction is still able to resolve some temporal information from a completely time-independent PIV measurement. The broadband spectral nature of the velocity field appears to inhibit the POD from extracting discrete frequencies.

Dynamic mode decomposition was also performed on the streamwise velocity of the LES, which cannot be similarly executed on PIV data due to the 10-Hz sampling rate. Figure 17(a) shows the peak frequencies and corresponding amplitudes from the DMD. A dominant peak is immediately evident in the 34-kHz region. Additional peaks are evident at 6, 10, 13, and 15 kHz, as well as harmonics of the 36-kHz frequency. As seen above (Fig. 16), POD was unable to isolate the events solely associated with the 34-kHz frequency, which stems from the inherent nature of the POD and DMD methodologies. In POD, the modes are ranked by the highest-variance features, thus the temporal coefficient of each mode may contain a variety of frequencies. Contrarily, DMD ranks modes by frequency and growth rate and each mode contains only a single frequency. Thus, for a flow field exhibiting distinct frequencies (i.e., 36 kHz), DMD will naturally identify the flow features attributed only to that frequency, whereas POD can produce this result, but the temporal coefficients are often broadband.

Figure 17(b) shows the spatial modes for a few of the peak frequencies identified previously. Dynamic mode decomposition is able to capture more coherent structures over the aft deck than the POD, which was also observed in [56] when examining different schlieren windows and orientations. The 5- and 6-kHz modes distinctly show the mixing layer and upper shear layer structures, while the 13- and 15-kHz modes identified smaller-scale structures in the upper shear layer, mixing layers, and downstream of the aft deck. These trailing edge structures are associated with entrainment and eventually convolve with the mixing layer.

Figure 18 shows the spatial correlation between the DMD and POD modes of the LES u-velocity field. It is clear that the DMD modes associated with the mixing layer and shear layer (between 10 and 15 kHz) are not contained in the high-energy POD modes. Additionally, the first two POD modes have strong correlations, between 40% and 60%, with the high-frequency DMD modes, but do not display such high-frequency content in the time-dependent coefficient spectra.

VIII. CONCLUSION

This study fused low-dimensional results from experimental and simulation data for a complex supersonic jet to reconstruct time-dependent POD coefficients. This reconstruction was first performed on schlieren data, due to aliasing of the dominant 34-kHz frequency as a result of the 50-kHz experimental sampling rate. In the reconstruction, the experimental POD basis functions were projected onto the LES snapshots to leverage both the statistical convergence of the experimental POD modes and the time resolution of the LES snapshots. The spectra of the reconstructed coefficients show the once aliased 14.7-kHz peak to be properly resolved at 34 kHz.

Dynamic mode decomposition was also applied to the experimental and numerical schlieren fields, and the spatial modes and temporal coefficients were compared to those obtained from POD. Similar flow structures and associated frequencies were observed using DMD, though the frequencies of the highest-amplitude DMD modes were slightly different from their POD counterparts.

Proper orthogonal decomposition was also utilized for the PIV and LES u-velocity fields. Despite the two data sets having a slightly different NTR, the first four modes of the POD had an almost identical spatial structure. The LES was also able to resolve structures along the aft deck that the PIV could not due to reflections from the laser. A reconstruction of the time-dependent POD coefficients was calculated using the spatial eigenfunctions of the PIV projected onto the LES velocity field. The spectra identified a slight peak around 34 kHz; however, the POD spectra of the velocity field were mostly broadband.

Dynamic mode decomposition was also applied to the LES u-velocity field. While POD was unable to extract distinct frequencies associated with the modes, several such modes could be extracted from DMD, namely, the 36-kHz signal along with its harmonics. Several other peaks could also be seen at lower frequencies. The high-amplitude DMD spatial modes highlighted different flow structures than POD. While the high-energy POD modes focused on large-scale structures in the shear layers, the dominant features in DMD were small structures in the shear layers and mixing layer. Such DMD modes associated with the mixing layer and shear layers were not correlated with the high-energy POD modes.

Reduced-order models can be leveraged in conjunction with data fusion techniques to merge information between data sets. This circumvents the limitations of experiments and simulations to generate a more complete view of the flow while also providing a basis for comparison. Continued analysis will allow for correlations between time-dependent near- and far-field pressure and the reconstructed velocity coefficients to identify which modes have the greatest impact on pressure fluctuations. This can provide insight into the turbulence mechanisms that promote noise generation and the subsequent propagation characteristics.

ACKNOWLEDGMENTS

The authors would like to acknowledge Air Force Office of Scientific Research for funding this research through Grant No. FA9550-15-1-0435. The authors would also like to acknowledge Dr. Christopher Ruscher, Spectral Energies, LLC, Phase II SBIR, with Dr. Alex Giese, Thomas Ferrill, and AFRL for the ongoing support and interactions throughout these research endeavors.

[1] J. L. Lumley, The structure of inhomogeneous turbulent flows, in *Atmospheric Turbulence and Radio Wave Propagation*, edited by A. M. Yaglom and V. I. Tatarsky (Nauka, Moscow, 1967), pp. 166–178.

[2] N. Aubry, P. Holmes, J. L. Lumley, and E. Stone, The dynamics of coherent structures in the wall region of a turbulent boundary layer, J. Fluid Mech. **192**, 115 (1988).
[3] M. N. Glauser, S. J. Leib, and W. K. George, Coherent structures in axisymmetric turbulent jet mixing layer, Turbul. Shear Flows **5**, 134 (1987).
[4] P. Moin and R. D. Moser, Characteristic eddy decomposition of turbulence in a channel, J. Fluid Mech. **200**, 471 (1989).
[5] G. Berkooz, P. Holmes, and J. L Lumley, The proper orthogonal decomposition in the analysis of turbulent flows, Annu. Rev. Fluid Mech. **25**, 539 (1993).
[6] L. Ukeiley, L. Cordier, R. Manceau, J. Delville, M. Glauser, and J.-P. Bonnet, Examination of large-scale structures in a turbulent plane mixing layer. Part 2. Dynamical systems model, J. Fluid Mech. **441**, 67 (2001).
[7] R. J. Adrian, On the role of conditional averages in turbulence theory, in *Proceedings of the Fourth Biennial Symposium on Turbulence in Liquids* (Science, Princeton, 1977), Vol. 66, pp. 323–332.
[8] R. J. Adrian, Particle-imaging techniques for experimental fluid mechanics, Annu. Rev. Fluid Mech. **23**, 261 (1991).
[9] D. R. Cole, M. N. Glauser, and Y. G. Guezennec, An application of the stochastic estimation to the jet mixing layer, Phys. Fluids A **4**, 192 (1992).
[10] L. Ukeiley, M. Glauser, and D. Wick, Downstream evolution of POD eigenfunctions in a lobed mixer, AIAA J. **31**, 1392 (1993).
[11] J. P. Bonnet, D. R. Cole, J. Delville, M. N. Glauser, and L. S. Ukeiley, Stochastic estimation and proper orthogonal decomposition: Complementary techniques for identifying structure, Exp. Fluids **17**, 307 (1994).
[12] J. Delville, E. Lamballais, and J. P. Bonnet, POD, LODS, and LSE: Their links to control and simulations of mixing layers, ERCOFTAC Bull. **46**, 29 (2000).
[13] C. E. Tinney, M. N. Glauser, and L. S. Ukeiley, Low-dimensional characteristics of a transonic jet. Part 1. Proper orthogonal decomposition, J. Fluid Mech. **612**, 107 (2008).
[14] C. E. Tinney, L. S. Ukeiley, and M. N. Glauser, Low-dimensional characteristics of a transonic jet. Part 2. Estimate and far-field prediction, J. Fluid Mech. **615**, 53 (2008).
[15] B. O. H. Jørgensen, Application of POD to PIV images of flow over a wall mounted fence, in *Proceedings of the IUTAM Symposium on Simulation and Identification of Organized Structures in Flows*, edited by J. N. Sørensen, E. J. Hopfinger, and N. Aubry, Fluid Mechanics and Its Applications Vol. 52 (Springer, Berlin, 1997), pp. 397–407.
[16] K. Cohen, S. Siegel, and T. McLaughlin, Feedback control of a cylinder wake low-dimensional model, AIAA J. **41**, 1389 (2003).
[17] J. T. Pinier, J. M. Ausseur, M. N. Glauser, and H. Higuchi, Proportional closed-loop feedback control of flow separation, AIAA J. **45**, 181 (2007).
[18] M. P. Wernet, Temporally resolved PIV for space-time correlations in both cold and hot jet flows, Meas. Sci. Technol. **18**, 1387 (2007).
[19] Z. P. Berger, P. R. Shea, M. G. Berry, B. R. Noack, S. Gogineni, and M. N. Glauser, Active flow control for high speed jets with large window PIV, Flow Turbul. Combust. **94**, 97 (2014).
[20] K. R. Low, Z. P. Berger, S. Kostka, B. El Hadidi, S. Gogineni, and M. N. Glauser, A low-dimensional approach to closed-loop control of a mach 0.6 jet, Exp. Fluids **54**, 1484 (2013).
[21] Z. P. Berger, M. G. Berry, P. R. Shea, M. N. Glauser, P. Kan, J. Lewalle, C. J. Ruscher, and S. P. Gogineni, Investigation of "loud" modes in a high-speed jet to identify noise-producing events, in *Proceedings of the 53rd AIAA Aerospace Sciences Meeting* (AIAA, Reston, 2015), paper 2015-0739.
[22] C.E. Tinney, P. Jordan, A. M. Hall, J. Delville, and M. N. Glauser, A time-resolved estimate of the turbulence and sound source mechanisms in a subsonic jet flow, J. Turbul. **8**, N7 (2007).
[23] M. Schlegel, B. R. Noack, P. Jordan, A. Dillmann, E. Groschel, W. Schröder, M. Wei, J. B. Freund, O. Lehmann, and G. Tadmor, On least-order flow representations for aerodynamics and aeroacoustics, J. Fluid Mech. **679**, 367 (2012).
[24] R. Zimmermann, A. Vendl, and S. Görtz, Reduced order modeling of steady flows subject to aerodynamic constraints, AIAA J. **52**, 255 (2014).

[25] C. J. Ruscher, J. F. Dannenhoffer III, and M. N. Glauser, Repairing occluded data for a Mach 0.6 jet via data fusion, AIAA J. **55**, 255 (2017).

[26] R. J. Simmons, Design and control of a variable geometry turbofan with an independently modulated third stream, Ph.D. thesis, The Ohio State University, 2009.

[27] A. S. Magstadt, M. G. Berry, P. R. Shea, M. N. Glauser, C. J. Ruscher, S. P. Gogineni, and B. V. Kiel, Aeroacoustic experiments on supersonic multi-aperture nozzles, in *Proceedings of the 51st AIAA/ASME/SAE/ASEE Joint Propulsion Conference, Orlando, 2015* (AIAA, Reston, 2015).

[28] M. G. Berry, A. S. Magstadt, and M. N. Glauser, Application of POD on time-resolved schlieren in supersonic multi-stream rectangular jets, Phys. Fluids **29**, 020706 (2017).

[29] G. S. Settles, *Schlieren & Shadowgraph Techniques* (Springer, Berlin, 2001).

[30] M. G. Berry, A. S. Magstadt, M. N. Glauser, C. J. Ruscher, S. P. Gogineni, and B. V. Kiel, An acoustic investigation of a supersonic, multi-stream jet with aft deck: Characterization and acoustically-optimal operating conditions, in *Proceedings of the 54th AIAA Aerospace Sciences Meeting* (AIAA, Reston, 2016), paper 2016-1883.

[31] C. E. Willert, D. M. Mitchell, and J. Soria, An assessment of high-power light-emitting diodes for high frame rate schlieren imaging, Exp. Fluids **53**, 413 (2012).

[32] S. Wilson, G. Gustafson, G. Lincoln, K. Murari, and C. Johansen, Performance evaluation of an overdriven led for high-speed schlieren imaging, J. Visual. **18**, 35 (2015).

[33] A. S. Magstadt, Investigating the structures of turbulence in a multi-stream, rectangular, supersonic jet, Ph.D. thesis, Syracuse University, 2017.

[34] D. V. Gaitonde and M. R. Visbal, High-order schemes for Navier-Stokes equations: Algorithm and implementation into FDL3DI, Air Force Research Laboratory Report No. AFRL-VA-WP-TR-1998-3060, 1998, http://www.dtic.mil/docs/citations/ADA364301.

[35] R. Speth and D. Gaitonde, Parametric study of a mach 1.3 cold jet excited by the flapping mode using plasma actuators, Comput. Fluids **84**, 16 (2013).

[36] D. Gaitonde and M. Samimy, Coherent structures in plasma-actuator controlled supersonic jets: Axisymmetric and mixed azimuthal modes, Phys. Fluids **23**, 095104 (2011).

[37] C. Bogey and C. Bailly, Influence of nozzle-exit boundary-layer conditions on the flow and acoustic fields of initially laminar jets, J. Fluid Mech. **663**, 507 (2010).

[38] D. P. Rizzetta and M. R. Visbal, Application of large eddy simulation to supersonic compression ramp, AIAA J. **40**, 1574 (2002).

[39] T. Lund, X. Wu, and K. Squires, Generation of turbulent inflow data for spatially-developing boundary layer simulations, J. Comput. Phys. **140**, 233 (1998).

[40] X. Xiao, J. Edwards, H. Hassan, and R. Baurle, Inflow boundary conditions for hybrid large-eddy/Reynolds-averaged Navier-Stokes simulations, AIAA J. **41**, 1481 (2003).

[41] H. Le, P. Moin, and J. Kim, Direct numerical simulation of turbulent flow over a backward-facing step, J. Fluid Mech. **330**, 349 (1997).

[42] P. Batten, U. Goldberg, and S. Chakravarthy, Interfacing statistical turbulence closures with large-eddy simulation, AIAA J. **42**, 485 (2004).

[43] M. Klein, A. Sadiki, and J. Janicka, A digital filter based generation of inflow data for spatially developing direct numerical or large eddy simulations, J. Comput. Phys. **186**, 652 (2003).

[44] E. Touber and N. D. Sandham, Oblique shock impinging on a turbulent boundary layer: Low-frequency mechanisms, in *Proceedings of the 38th Fluid Dynamics Conference and Exhibit* (AIAA, Reston, 2008), paper 2008-4170.

[45] C. M. Stack and D. V. Gaitonde, Dynamical features of a supersonic multistream nozzle with an aft-deck, in *Proceedings of the 55th AIAA Aerospace Sciences Meeting* (AIAA, Reston, 2017), paper 2017-0557.

[46] M. G. Berry, C. M. Stack, M. Y. Ali, A. S. Magstadt, D. V. Gaitonde, and M. N. Glauser, Analysis of a rectangular supersonic multi-stream jet by LES and experiments, in *Proceedings of the Tenth International Symposium on Turbulence and Shear Flow Phenomena* (TSFP, 2017), http://tsfp10.org/TSFP10_program/2/389.pdf.

[47] L. Sirovich, Turbulence and the dynamics of coherent structures Part I: Coherent structures, Q. Appl. Math. **45**, 561 (1987); Turbulence and the dynamics of coherent structures Part II: Symmetries and

transformations, *ibid.* **45**, 573 (1987); Turbulence and the dynamics of coherent structures Part III: Dynamics and scaling, *ibid.* **45**, 583 (1987).

[48] S. Park, A. Wachsman, A. Annaswamy, A. Ghoniem, B. Pang, and K. Yu, Experimental study of POD-based control for combustion instability using a linear photodiode array, in *Proceedings of the 42nd AIAA Aerospace Sciences Meeting* (AIAA, Reston, 2004), paper 2004-639.

[49] C. Alvarez-Herrera, D. Moreno-Hernández, and B. Barrientos-García, Temperature measurement of an axisymmetric flame by using a schlieren system, J. Opt. A **10**, 104014 (2008).

[50] S. Tsutsumi, T. Nonomura, K. Fujii, Y. Nakanishi, K. Okamoto, and S. Teramoto, Analysis of acoustic wave from supersonic jets impinging to an inclined at plate, in *Proceedings of the Seventh International Conference on Computational Fluid Dynamics* (Springer, Berlin, 2012), paper ICCFD7-3104.

[51] T. Ecker, D. R. Brooks, K. T. Lowe, and W. F. Ng, Quantitative image processing of high-speed schlieren of a hot supersonic jet, in *Proceedings of the 66th Annual Meeting of the APS Division of Fluid Dynamics* (APS, New York, 2013), Vol. 59.

[52] C. W. Rowley, I. Mezic, S. Bagheri, P. Schlatter, and D. S. Henningson, Spectral analysis of nonlinear flows, J. Fluid Mech. **641**, 115 (2009).

[53] P. J. Schmid, Dynamic mode decomposition of numerical and experimental data, J. Fluid Mech. **656**, 5 (2010).

[54] A. Ruhe, Rational Krylov sequence methods for eigenvalue computation, Linear Algebra Appl. **58**, 391 (1984).

[55] A. S. Magstadt, M. G. Berry, T. J. Coleman, P. R. Shea, M. N. Glauser, C. J. Ruscher, S. P. Gogineni, and B. V. Kiel, A near-field investigation of a supersonic, multi-stream jet: locating turbulence mechanisms through velocity and density measurements, in *Proceedings of the 54th AIAA Aerospace Sciences Meeting* (AIAA, Reston, 2016), paper 2016-1639.

[56] M. G. Berry, Y. M. Ali, A. S. Magstadt, and M. N. Glauser, DMD and POD of time-resolved schlieren on a multi-stream single expansion ramp nozzle, Int. J. Heat Fluid Flow **66**, 60 (2017).